GSA Data Repository 2020126

ADDITIONAL DETAILS ON METHODS AND RESULTS

Table of Contents

Topographic data

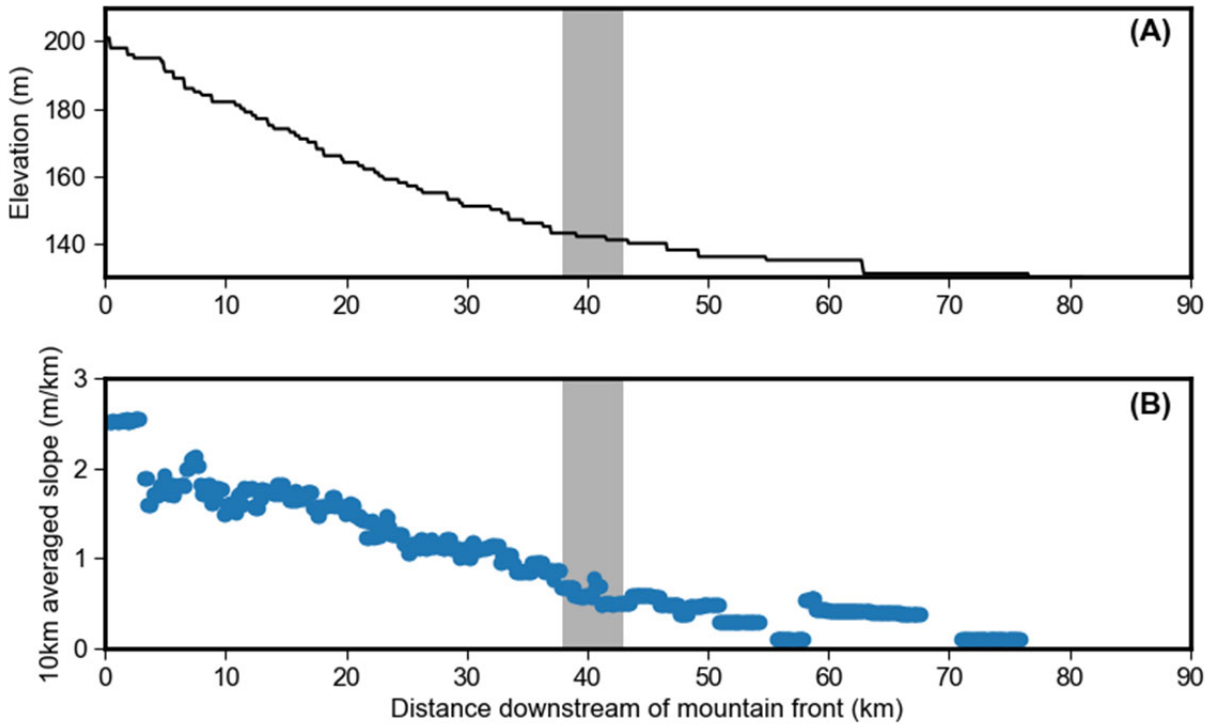

Figure DR1. A) Karnali longitudinal channel profile downstream of the mountain front (at Chisapani) extracted from 30 m Shuttle Radar Topographic Mission (SRTM) Digital Elevation Model (DEM). The profile has been extracted for the west branch along which our measurements have been carried out. The position of the gravel-sand transition is shown by the vertical grey box. B) 10 km averaged slope values downstream of the Himalayan mountain front derived from the same DEM.

Suspended Sediment and Acoustic Doppler Current Profile (ADCP) Transect Details

Sampling locations were selected by identifying the channel thalweg, maximum channel depth and cross-sectional flow velocity and discharge in cross-sections using a Sontek M9 acoustic Doppler current profiler (ADCP) mounted with an RTK-GPS system (Fig. DR2.1-2.5). To calculate discharge and velocity, two to four ADCP transects were made at each site; all were found to have comparable discharges (<5 % difference between repeat transects). Samples were collected in a 5 litre horizontal Van Dorn water sampler while floating downstream with the sampler at a constant depth below the water surface. Each water and sediment sample in a vertical was collected from approximately the same location, where the channel was the deepest and where flow was not obviously dominated by secondary currents or significant upwelling. Each sample was filtered and dried to retain the sediment grain size fraction >0.5 µm (which was the mesh size of our filters). Grain size distributions between 0.5 and 2000 µm were measured in Edinburgh University using a laser diffractometer (Beckmann Coulter LSD230).

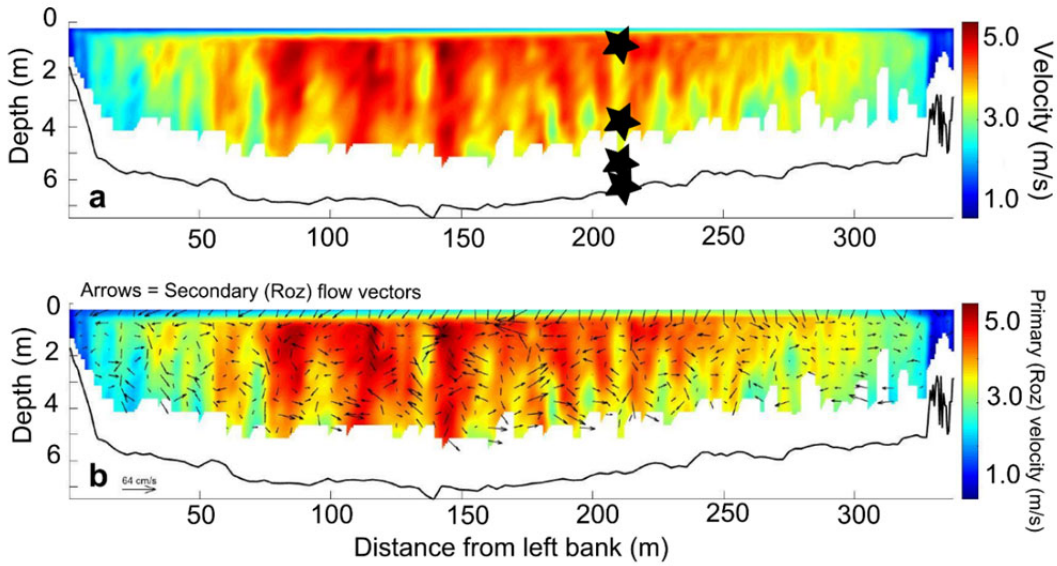

Figure DR2.1 Acoustic Doppler Current Profile (ADCP) transect at T1 using the Velocity Mapping Toolbox (VMT) v4.08 (Parsons et al., 2013) software showing a) absolute (stream wise + transverse) velocity and approximate suspended sediment point samples (black stars), and b) both primary velocity (colors) and secondary (arrows) flow components (Rozovskii method). Arrow length is scaled to measured secondary flow velocity. A net secondary flow velocity of 0.64 m/s directed towards the right bank is observed, likely due to the slight curvature of the channel.

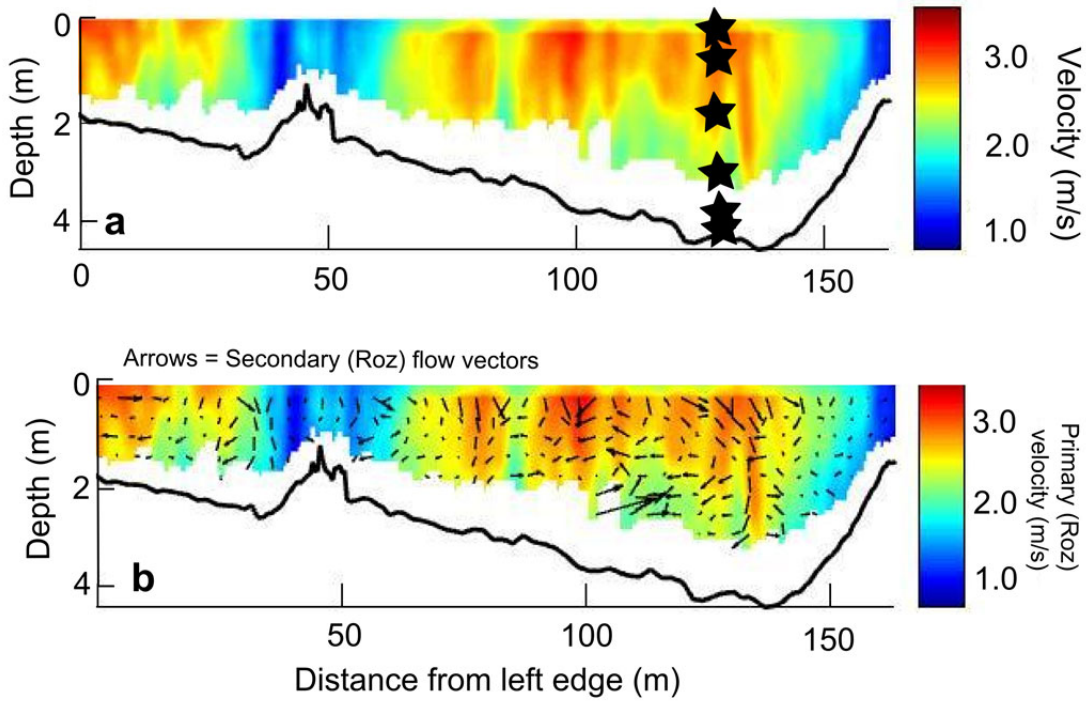

Figure DR2.2 Acoustic Doppler Current Profile (ADCP) transect at T2 using the Velocity Mapping Toolbox (VMT) v4.08 (Parsons et al., 2013) software showing a) absolute (stream wise + transverse) velocity and approximate suspended sediment point samples (black stars), and b) both primary velocity (colors) and secondary (arrows) flow components (Rozovskii method). Arrow length is scaled to measured secondary flow velocity.

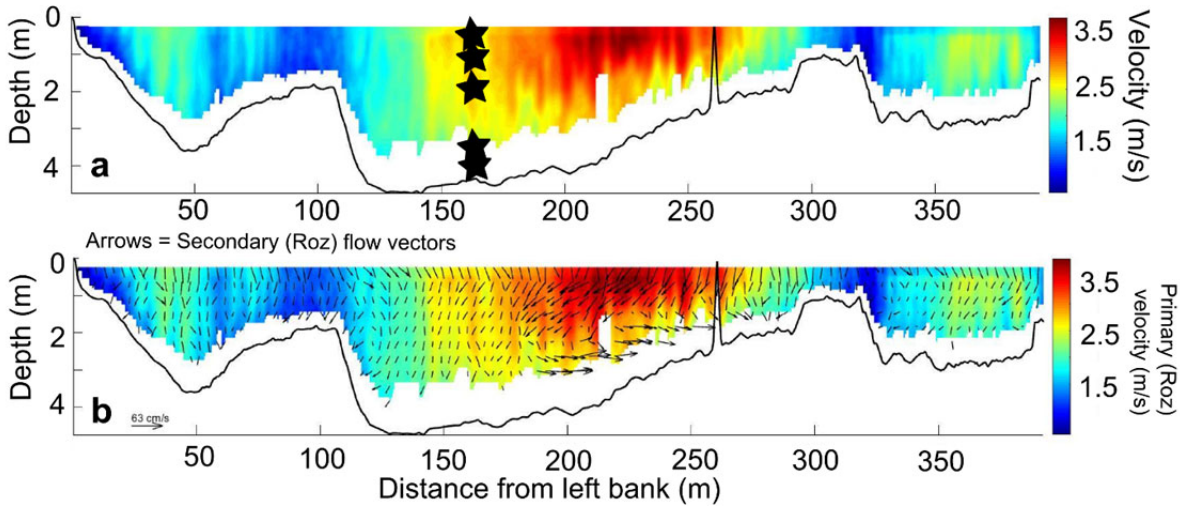

Figure DR2.3 Acoustic Doppler Current Profile (ADCP) transect at T3 using the Velocity Mapping Toolbox (VMT) v4.08 (Parsons et al., 2013) software showing a) absolute (stream wise + transverse) velocity and approximate suspended sediment point samples (black stars), and b) both primary velocity (colors) and secondary (arrows) flow components (Rozovskii method). Arrow length is scaled to measured secondary flow velocity. A net secondary flow velocity of 0.63 m/s directed towards the right bank is observed, likely due to the slight curvature of the channel.

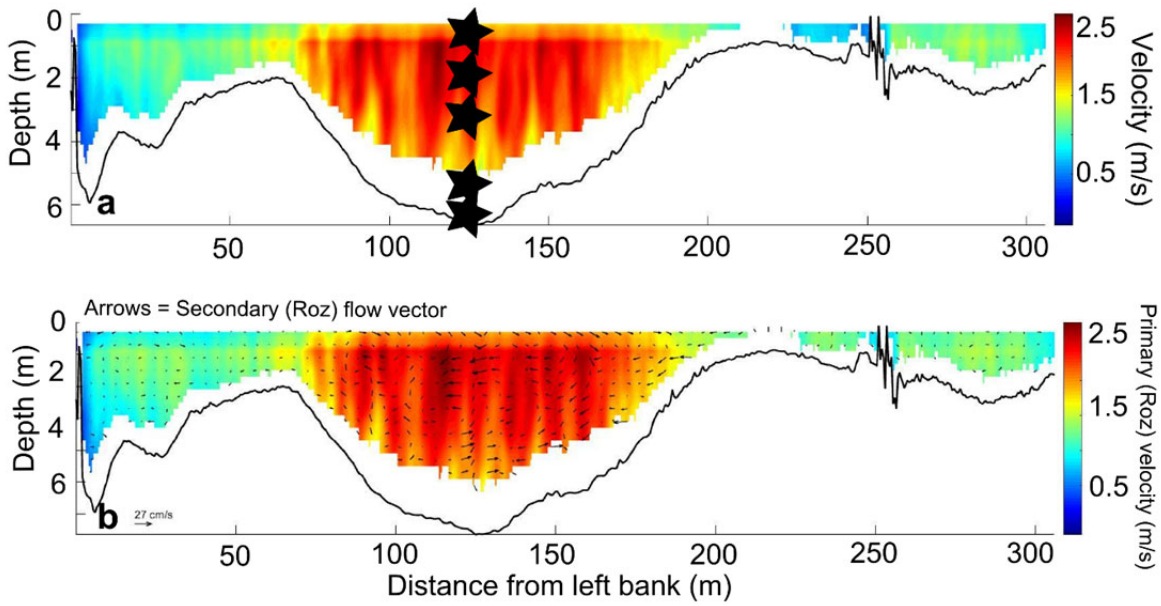

Figure DR2.4 Acoustic Doppler Current Profile (ADCP) transect at T4 using the Velocity Mapping Toolbox (VMT) v4.08 (Parsons et al., 2013) software showing a) absolute (stream wise + transverse) velocity and approximate suspended sediment point samples (black stars), and b) both primary velocity (colors) and secondary (arrows) flow components (Rozovskii method). Arrow length is scaled to measured secondary flow velocity. A net secondary flow velocity of 0.27 m/s directed towards the right bank is observed, likely due to the slight curvature of the channel.

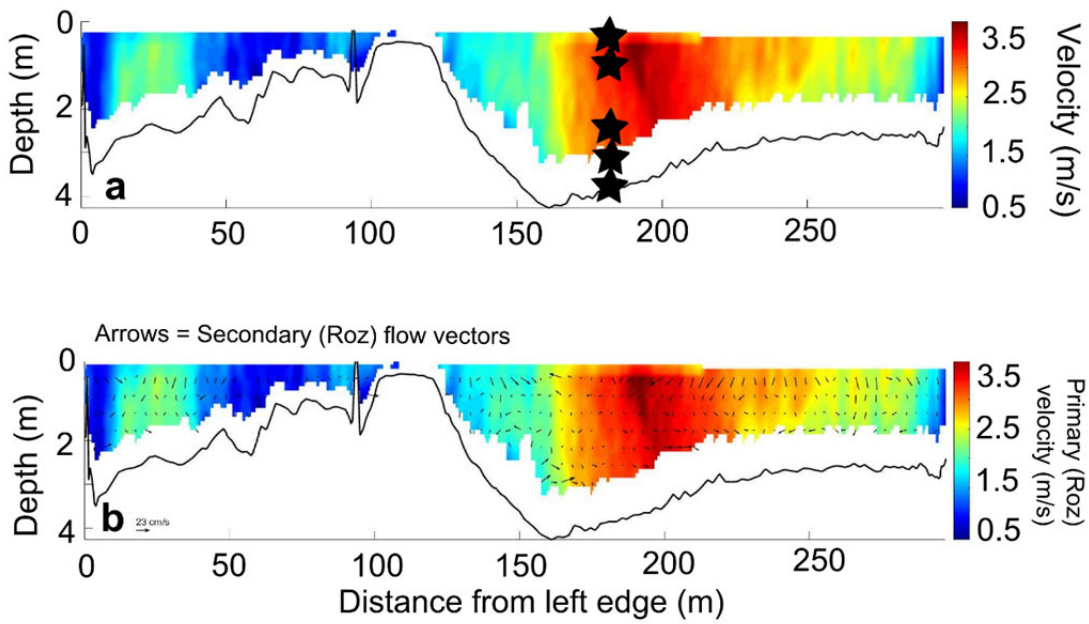

Figure DR2.5 Acoustic Doppler Current Profile (ADCP) transect at T5 using the Velocity Mapping Toolbox (VMT) v4.08 (Parsons et al., 2013) software showing a) absolute (stream wise + transverse) velocity and approximate suspended sediment point samples (black stars), and b) both primary velocity (colors) and secondary (arrows) flow components (Rozovskii method). Arrow length is scaled to measured secondary flow velocity. A net secondary flow velocity of 0.23 m/s directed towards the right bank is observed, likely due to the slight curvature of the channel.

Instantaneous Sediment Flux Calculations

Instantaneous sediment flux was calculated using two methods to ensure the results were robust and not contingent on the method used. We first calculated flux as the product of depth-averaged concentration in the vertical and ADCP discharge measurement Q_{ADCP}. We also calculated suspended sediment flux from the grain size specific Rouse equation:

$$\frac{c_{zi}}{c_{ai}} = \left(\frac{h-z}{a} - \frac{a}{h-a}\right)^{R_{0i}} , \qquad (1)$$

where c_{zi} is the concentration at height above the bed z of grain size class i, c_{ai} is a reference concentration of grain size class i, measured at height a of the lowest suspended sediment sample, and h is maximum depth. R_{0i} is the Rouse number calculated as:

$$R_{0i} = \frac{w_{si}}{\beta \kappa u^*} , \qquad (2)$$

where w_{si} is the sediment fall velocity calculated from Dietrich (1982) for grain size class i, β is a coefficient that describes the difference in diffusion between a sediment particle and a fluid particle (assumed to be 1), κ is the von Karman constant (0.41) and u^* is the shear velocity calculated using the ADCP-measured velocity profile at the suspended sediment measurement location. Ideally, measurements from the lowest 20% of the water column would have been used, but in two instances there were insufficient data points from this depth to derive a reasonable $u*$ value. For consistency, $u*$ was calculated using the full velocity profile at each location (Table DR1). Taking our velocity profiles, $u*$ was calculated using the best-fit relationship between velocity (v) and height above the bed (z) where:

$$v = \alpha \ln(z) + b, \qquad (3)$$

$$u_* = \kappa\alpha, \qquad (4)$$

Table DR1. Calculated u_* values at sites on the Karnali River

Site	u_* (m/s)
T1	0.287
T2	0.224
T3	0.178
T4	0.214
T5	0.113

The depth-averaged concentration from the Rouse profiles was calculated by summing the grain size specific concentration profiles at each elevation above the bed, then taking the depth-weighted average of the summed profiles. The sediment flux from the Rouse profiles and the measurements was calculated by multiplying the depth-averaged concentration by Q_{ADCP} to give the total sediment flux in the channel.

The Rouse profile calculation predicted the vertical distribution of finer size classes well, but the coarsest size fractions were underpredicted, particularly at T1. The underprediction suggests enrichment of coarse bed material in the water column. At T1, there is strong upwelling as flow exits a canyon (e.g. Venditti et al, 2014). The underpredictions make the Rouse profile sediment fluxes marginally less than the calculations using the measurements, but the effect is small because concentrations of coarse sand in suspension are small. We regard the Rouse profile sediment fluxes as more reliable than the measurements because it removes variability in the profile that is probably not representative of the mean concentration profile and it removes that strong likelihood of error or bias in the single sediment samples. Gitto et al. (2017) showed that the probability of measuring the mean concentration and grain size with a 30-second, point-

integrated, isokinetic sampler is 30-40%. With an instantaneous Van Dorn grab sample, the likelihood of capturing the mean concentration and grain size is even less. Hence our reliance on the Rouse profile sediment fluxes. Nevertheless, the patterns in the sediment fluxes are the same for both methods.

.

Sediment Dating by Optically Stimulated Luminescence (OSL)

Sampling was undertaken by the authors H.D.S. and L.Q. in April 2017. Samples were submitted for analysis at the Luminescence Laboratories within the School of Earth and Environmental Sciences at the University of St Andrews. A luminescence age is the quotient of the equivalent dose (De, in Gy), a laboratory estimate of the accumulated dose through time, and the environmental dose rate (mGy a^{-1}), the rate at which ionising radiation is delivered to the sample. The following sections describe the methods used to determine De, estimate the dose rate, and calculate sediment ages.

De Determinations

Standard mineral preparation procedures as routinely used in Optically Stimulated Luminescence (OSL) dating were used to extract sand-sized quartz from each sample (cf. Kinnaird et al., 2017). De determinations were made on sets of 32 aliquots of 150-250 µm, 2.64-2.74 g cm^{-3}, HF-etched quartz, using a single-aliquot regenerative dose (SAR) method (Kinnaird et al., 2017; Murray and Wintle, 2000). All OSL measurements were undertaken on a Risø TL/OSL DA-20 automated dating system. OSL was detected through 7.5 mm of Huoya U-340 filter with a 9635QA photomultiplier tube. OSL was measured at 125°C for 60 seconds. The SAR technique involves making a series of paired measurements of OSL intensity - Ln and Lx, and the response to a fixed test dose, Tn and Tx. Each measurement is standardised to the test dose response determined immediately after its readout, to compensate for observed changes in sensitivity during the laboratory measurement sequence. De values are then estimated using the corrected OSL intensities Ln/Tn and Lx/Tx and the interpolated dose-response curve. This was

implemented here using up to seven regenerative doses (nominal doses of 1, 2.5, 5, 10, 20, 50 and 150 Gy), with additional cycles for zero dose, repeat or 'recycling' dose and IRSL dose. Data reduction and De determinations were made in Luminescence Analyst v.4.31.9. Individual decay curves were scrutinised for shape and consistency. Dose response curves were fitted with an exponential function, with the growth curve fitted through zero and the repeat recycling points. Error analysis was undertaken by Monte Carlo stimulation. Aliquots were rejected from further analysis if they failed sensitivity checks (based on test dose response), SAR acceptance criteria checks, or had significant IRSL response coupled with anomalous luminescence behaviour.

Figure DR3.1 illustrates representative OSL decay curves for CERSA069 (OSL6) and the corresponding dose response curve. The OSL signal from the first 2.4 s was used for analysis, with a background subtracted from the last 9.6 s. Figure DR3.2 shows the corresponding Kernel Density Estimate (left) and Abanico (right) plots for this sample's De distribution. Scatter varied between samples.

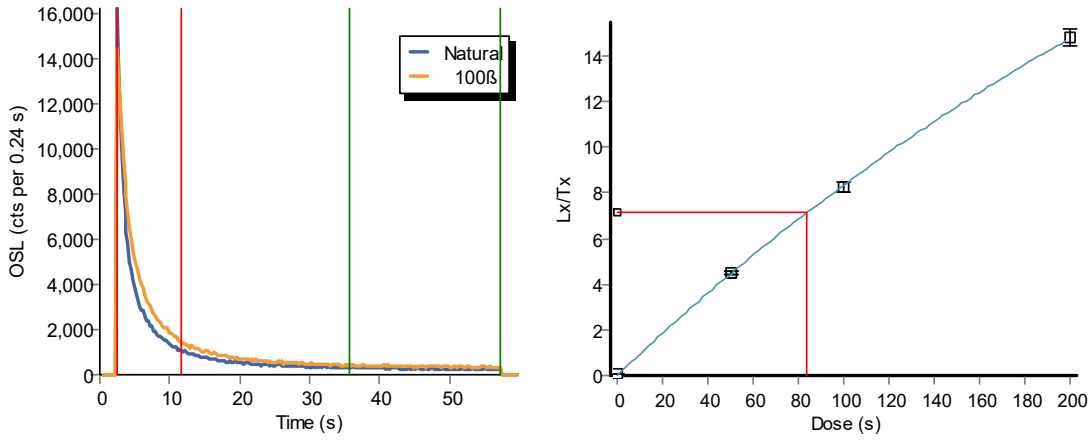

Figure DR3.1. Representative decay (left) and dose response (right) curves as obtained for CERSA069 (OSL6).

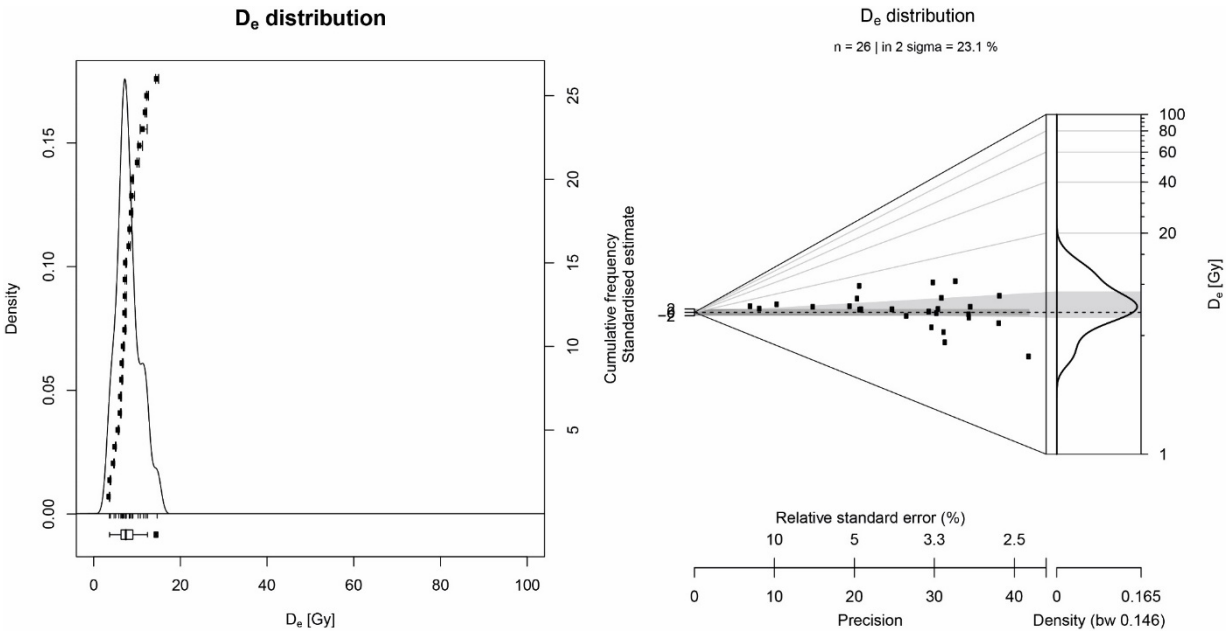

Figure DR3.2. De distributions for CERSA069 (OSL6) plotted as (left) Kernel Density Estimate and (right) Abanico plots (after Dietze et al., 2013).

Dose rate determinations

Concentrations of K, U, Th and Rb were measured directly using ICPMS. These data were used to determine infinite matrix doses for α, γ and β radiation, using the conversion factors of Guérin et al. (2011), grain-size attenuation factors of Mejdahl (1979), and attenuating for sediment-matrix water content. Fractional and saturated water contents were determined for all samples in the laboratory. Fractional water contents were extremely varied, ranging between c. 1 and 30% of dried weight, reflecting the position of the collected sample relative to the water table. Saturated water contents were around 30% of dried weight. Working values of between 14 and

28 ± 5% were adopted for effective dose rate evaluation. The contribution from the cosmic dose, which is a function of geographic location and burial depth, was calculated from Prescott and Hutton (1994). The total effective dose rate to the HF-etched quartz was found to range between 2.60 and 4.17 mGy a^{-1} (Table DR2.1).

Table DR2.1 Total effective dose rates to HF-etched Quartz

[a]*Effective beta dose rate combining water content corrections with grain size attenuation factors*

Laboratory code	Field Code	Assumed water content (%)	Effective Beta dose rate[a] (mGy a^{-1})	Effective Gamma dose rate (mGy a^{-1})	Cosmic Dose rate contribution (mGy a^{-1})	**Total effective dose rate (mGy a^{-1})**
CERSA66	OSL3	23 ± 5	2.23 ± 0.12	1.57 ± 0.01	0.19 ± 0.02	3.99 ± 0.12
CERSA67	OSL4	28 ± 5	2.08 ± 0.10	1.52 ± 0.01	0.19 ± 0.02	3.78 ± 0.11
CERSA68	OSL5	26 ± 5	1.87 ± 0.10	1.28 ± 0.01	0.2 ± 0.02	3.36 ± 0.10
CERSA69	OSL6	18 ± 5	2.01 ± 0.11	1.62 ± 0.01	0.2 ± 0.02	3.83 ± 0.11
CERSA70	OSL7	17 ± 5	2.19 ± 0.12	1.68 ± 0.01	0.19 ± 0.02	4.05 ± 0.12

Age calculations

Equivalent dose distributions were reduced to a burial dose, Db, the radiation dose experienced by the sediments since their last zeroing event assumed to be exposure to light prior to final deposition. It is recognised that fluvial sediments have the potential to enclose mixed age sediments, due to variable bleaching at deposition; with such sediments, it can be argued that the low dose populations represent the better bleached components, and the tail to higher apparent doses the incompletely bleached component. Three of the dating samples (OSL3, OSL6 and OSL7) are characterised by moderately tight distributions, representing the better bleached sediments; for these, the weighted mean estimate of apparent dose adequately encloses the burial dose. One of the samples (OSL5) is characterised by a wide distribution, and as for the latter

samples, the low-dose component was assumed to enclose the burial dose. For these samples, the high-dose outliers were removed from further analysis; however, the larger weighted standard deviations for these samples reflect the greater spread in equivalent dose values. Table DR2.2 lists the sediment burial ages for these samples.

Table DR2.2. Sediment burial ages

Laboratory code	Field ID	Burial dose (Gy)	Age (ka)
CERSA66	OSL3	3.40 ± 1.23 (0.04)	0.85 ± 0.31 (0.05)
CERSA67	OSL4	1.85 ± 0.56 (0.11)	0.49 ± 0.15 (0.03)
CERSA68	OSL5	8.59 ± 4.09 (0.09)	2.56 ± 1.22 (0.17)
CERSA69	OSL6	5.65 ± 1.56 (0.04)	1.47 ± 0.41 (0.09)
CERSA70	OSL7	16.58 ± 2.12 (0.12)	4.09 ± 0.54 (0.22)

Thresholds of Sediment Entrainment

The critical discharge (Q_c) was calculated as:

$$Q_c = Uh_cW = C\sqrt{h_cS}h_cW \quad , \qquad (5)$$

where U is flow velocity, W is channel width (bankfull), S is channel gradient and h_c is the critical flow depth. The modified Chezy coefficient (C) is defined as;

$$C = 8\left(\frac{h_c}{2D_{90}}\right)^{\frac{1}{6}}\sqrt{g} \quad , \qquad (6)$$

where g is gravitational acceleration and D_{90} is the 90th percentile of the grain size distribution. h_c was calculated using two methods for sand and gravel-bed reaches, respectively. For the sand-bed channel, h_c was calculated for the median grain size (D_{50}) using a critical Shields number (τ_c^*) of 0.03 and a form drag correction β = 0.5 (Venditti and Church, 2014);

$$h_c = \frac{\tau_c^*(\rho_s - \rho_w)D_{50}}{\beta\rho_w S} \quad , \qquad (7)$$

For the gravel-bed channel, we assumed a slope-dependent τ_c^* (Lamb et al., 2008) such that:

$$h_c = \frac{0.15(\rho_s - \rho_w)D_{50}}{\beta S^{0.75}\rho_w} \quad , \qquad (8)$$

where ρ_w and ρ_s are the density of water and sediment respectively. Values of β reported in Venditti and Church (2014) for gravel-bed channels vary between 0.5 and 0.6.

Grain Size Sampling

Photos were taken of two gravel bar surfaces that are exposed under all but the largest monsoonal flows at the apex of the gravel island that marks the Karnali bifurcation ("gravel bar"). Photos were also taken form the dry river bed exposed at the bifurcation at low flow ("gravel bed") (Fig. DR4 for detailed description). Particle sizes were measured from each photo by overlaying a numeric square grid with 100 nodes and measuring the intermediate *b*-axis of each pebble beneath the nodes (Attal and Lavé, 2006; Whittaker et al. 2011).

Table DR3. Details of grain size samples and grain size statistics.

Sample	***Date***	***Location***	***Details***	D_{50} ***(mm)***	D_{90} ***(mm)***
Gravel bar	25th October 2016	28.599792 81.259463	Surface grain size from central bar at Karnali bifurcation	65	155
Gravel bed	5th April 2017	28.601396 81.261771	Exposed gravel bed material at bifurcation	231	418
Sand bank	7th April 2017	28.417784 81.043490	Bank material downstream of the gravel-sand transition	0.23	0.36
Sand bed	21st August 2017	28.420623 81.051930	Bed material dredged at transect T5	0.31	0.89

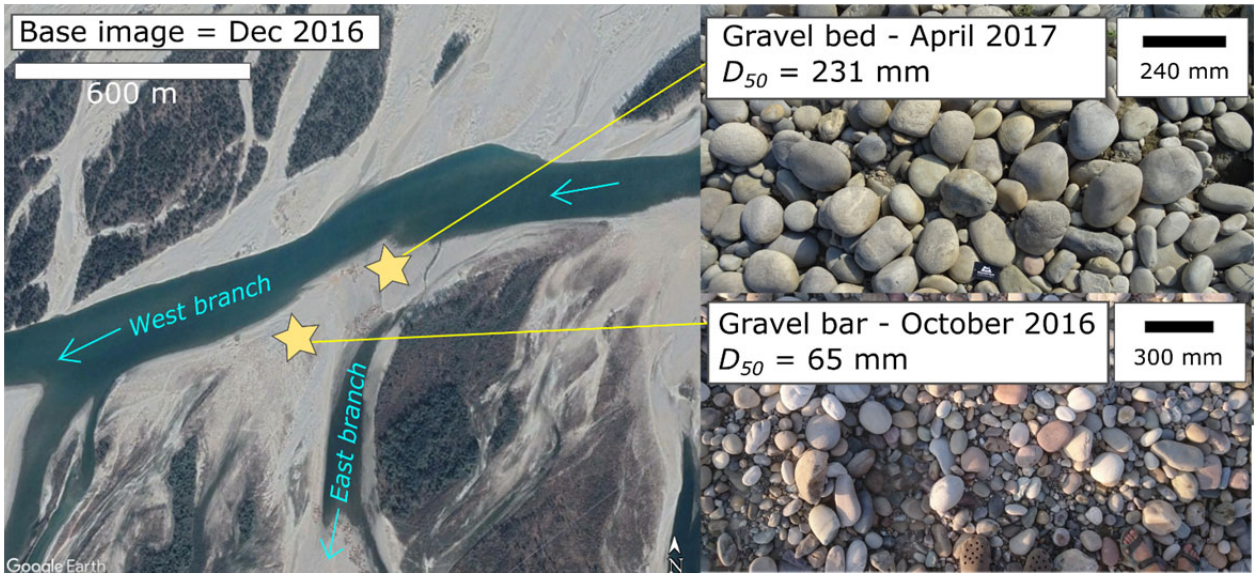

Figure DR4. Gravel grain size sampling locations at the Karnali bifurcation (see Table DR3 for lat/lon). The sample taken from the surface of the 'gravel bar' is from the surface of the bifurcation bar exposed in October 2016. Flow depth in the west branch was ~4 m while flow into the east branch was only 1-2 m in depth. As flow levels receded between October and December 2016, the 'gravel bed' became exposed at the bifurcation point ('gravel bed' star on figure). This body of gravel appears to act as a plug or lip into the east branch, where flow must be of certain depth in the main (or west) channel before it spills into the east branch. In April 2017, water levels were low enough that the 'gravel bed' location was exposed and grain size measurements were made on this coarser material. During low flow conditions, the east branch appears to be fed by subsurface percolation through this plug.

Channel Migration

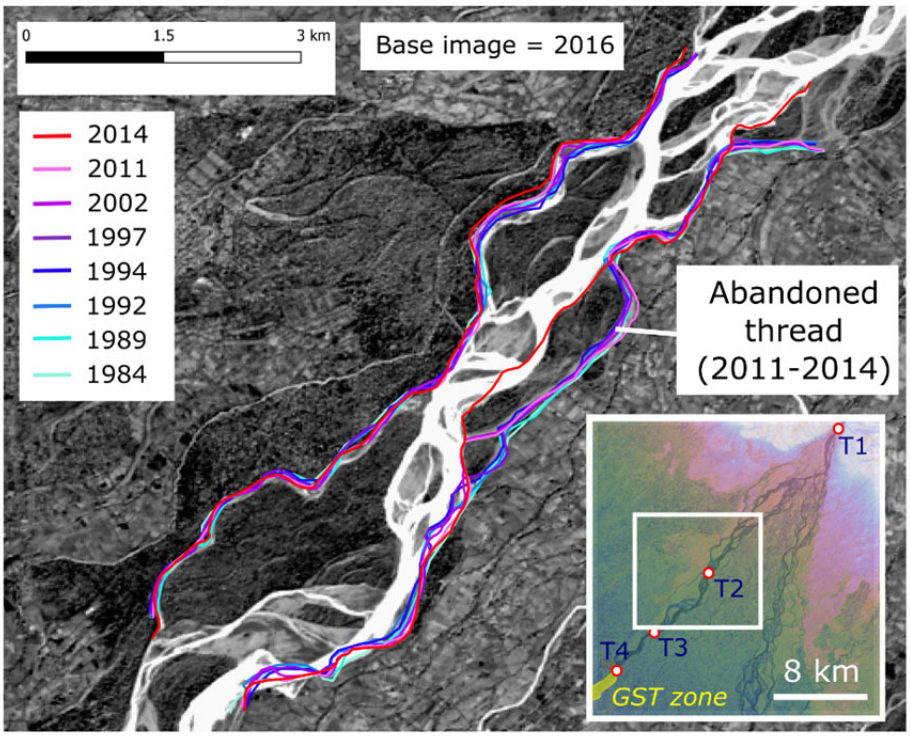

Figure DR5.1 Example of channel migration upstream of the Karnali gravel-sand transition, documented from LandSat satellite images between 1984 and 2016. The majority of scenes were captured between October and April where water levels were fairly comparable. The bottom right inset shows the extent of the images used relative to the gravel-sand transition and suspended sediment sampling locations. The base image shown is from 2016. The different coloured lines represent the position of the braided channel belt for each year analysed (indicated in the legend). The only significant change is the abandonment of a single thread between 2011 and 2014. In general, the position of the channel belt is stable, although there is obvious thread switching and reworking of gravel bars between images. This is not shown here due to the lower

resolution of the earlier satellite imagery (>30 m): images are too coarse to accurately identify individual braid channels within the channel belt.

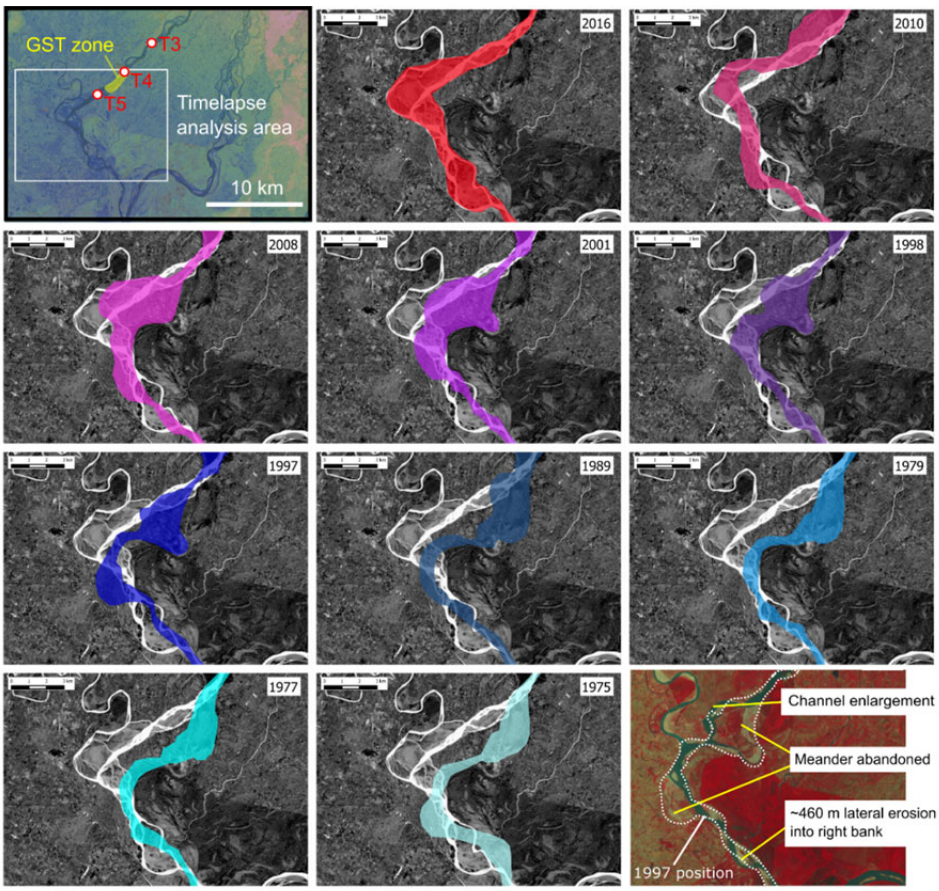

Figure DR5.2 Example of lateral channel migration downstream of the Karnali gravel-sand transition, documented from LandSat satellite images between 1975 and 2016. The majority of scenes were captured between October and April where water levels were fairly comparable. The top left panel shows the extent of the images used relative to the gravel-sand transitions and suspended sediment sampling locations. The base image shown in each panel is from 2016. The different coloured polygons represent the position of the channel belt for each year (indicated in the top right of each panel). In the bottom right panel, the base image is from 1998 and the position of the 1997 channel is shown by the white dashed lines. Over the course of a single year

(1997-1998), up to ~460 m of outer bank erosion occurs along sections of the channel. Between images separated by multiple years, kilometre-scale migration of smaller thread-channel meander apexes occurs.

2007 Fraser River Gravel-Sand Transition Sampling

Table DR4. 2007 Fraser River sediment sampling

	Total Suspended flux (t/d)	Sand suspended flux (t/d)	Bed load flux (t/d)	Total sand load (t/d)	Ratio of bed load sand to suspended sand (%)
Fraser River (immediately upstream of GST) 49.14132 (lat) -122.174 (lon)	94,568	40,047	1609	41,656	4
Fraser River (15 km downstream of GST) 49.13687 (lat) -122.280 (lon)	171,267	117,502	14,567	126,952	8

Following a peak spring freshet flow (11,800 m^3/s) in June 2007, bed load, assessed from repeat multibeam maps of dune fields (Venditti et al., 2019), and measured suspended sediment flux were made at two cross-sections separated by 9 kilometers in the diffuse extension of the Fraser River gravel sand transition (GST). The flux of mud (<0.063 mm) was 0.054 Mt/d and did not change in the downstream direction, because mud is transported as wash load in both the gravel and sand reaches. The total flux of sand (bed load plus suspended load) increased downstream from 41,656 t/d to 126,952 t/d, a trend that was also observed in the Karnali. Bed load was ten times greater at the downstream site, as the total load fraction carried on the bed increased from 4% to 8%. In the Fraser River, the increase in sediment flux occurs because sand stored on the bed at the upstream limit of the GST is evacuated during high flows and deposited downstream in the diffuse extension of the GST (Venditti et al., 2015). Sand is transferred from suspension to

the bed in the downstream direction, increasing the sand supply to the bed (and therefore the fraction of sand transported as bed load) and making larger bedforms (Venditti et al., 2019). Long-term monitoring records, at stations upstream and downstream of the GST, show of sediment flux is identical, suggesting that the downstream increase in sediment concentration is temporary (see McLean et al., 1999 for sediment flux records).

ADDITIONAL REFERENCES CITED

Dietrich, W.E., 1982, Settling velocity of natural particles: Water Resources Research, v. 18, p. 1615–1626, doi:10.1029/WR018i006p01615.

Dietze, E., Wünnemann, B., Hartmann, K., Diekmann, B., Jin, H., Stauch, G., Yang, S., and Lehmkuhl, F., 2013, Early to mid-Holocene lake high-stand sediments at Lake Donggi Cona, northeastern Tibetan Plateau, China: Quaternary Research, v. 79, p. 325–336, doi:10.1016/j.yqres.2012.12.008.

Gitto, A.B., J.G. Venditti, R.A. Kostaschuk and M. Church (2017). Representative Point-Integrated Suspended Sediment Sampling in Rivers. Water Resources Research, v. 53, p. 2956–2971, doi:10.1002/2016WR019187.

Guérin, G., Mercier, N., and Adamiec, G., 2011, Dose-rate conversion factors: update. Ancient TL, v. 29(1), p. 5-8.

Kinnaird, T.C., Dawson, T. C., Sanderson, D., Hamilton, D., Cresswell, A., and Rennell, R., 2017, Chronostratigraphy of an eroding complex Atlantic Round House, Baile Sear,

Scotland: The Journal of Coastal and Island Archaeology, v. 14(1), p. 46-60, doi:10.1080/15564894. 2017.1368744

McLean, D.G., Church, M. and Tassone, B., 1999. Sediment transport along lower Fraser River: 1. Measurements and hydraulic computations. Water Resources Research, v. 35(8), p. 2533-2548.

Mejdahl, V., 1979. Thermoluminescence dating: beta-dose attenuation in quartz grains. Archaeometry, v. 21(1), p.61-72.

Murray, A.S., and Wintle, A.G., 2000, Luminescence dating of quartz using an improved single-aliquot regenerative-dose protocol: Radiation Measurements, v. 32, p. 57–73, doi:10.1016/S1350-4487(99)00253-X.

Parsons, D.R., Jackson, P.R., Czuba, J.A., Engel, F.L., Rhoads, B.L., Oberg, K.A., Best, J.L., Mueller, D.S., Johnson, K.K., and Riley, J.D., 2013, Velocity Mapping Toolbox (VMT): a processing and visualization suite for moving-vessel ADCP measurements: Earth Surface Processes and Landforms, v. 38, p. 1244–1260, doi:10.1002/esp.3367.

Prescott, J.R. and Hutton, J.T., 1994. Cosmic ray contributions to dose rates for luminescence and ESR dating: large depths and long-term time variations. Radiation measurements, v. 23(2-3), p.497-500.

Venditti , J.G., C.D. Rennie, J. Bomhof, R.W. Bradley, M. Little, M. Church (2014), Flow in bedrock canyons, Nature, v. 513, p. 534-537. doi:10.1038/nature13779.